Geomechanics and Engineering, *Vol. 26, No. 3 (2021) 275-288*
https://doi.org/10.12989/gae.2021.26.3.275

Hydromechanical behavior and prediction of unsaturated loess over a wide suction range

Tong Jiang, Jindi Zhao, Junran Zhang*, Lijin Wang, Chenyu Song and Tianya Zhai

Henan Province Key Laboratory of Geomechanics and Structural Engineering,
North China University of Water Resources and Electric Power, Zhengzhou, Henan 450045, China

(Received March 29, 2021, Revised June 29, 2021, Accepted August 3, 2021)

Abstract. Subgrade loess in arid and semi-arid regions subjected to high-suction conditions owing to low relative humidity and deep groundwater levels. Understanding the hydromechanical behavior of unsaturated compacted loess over a wide suction range is critical for resolving infrastructure problems in such areas. In this study, the water retention behavior of loess was investigated by imposing or measuring suction (s) using the axis translation technique, vapor equilibrium technique, and chilled mirror dew point technique. Triaxial tests were also performed to study the mechanical behavior of compacted loess under different net cell pressures (σ_{3n}). The soil-water retention curves obtained using the different techniques are consistent. The degree of saturation and water content decreases significantly when s < 240 kPa, whereas the change of void ratio is relatively small. The water content versus s curves with different initial dry densities is coincident when s > 0.5 MPa, indicating that undrained triaxial tests can be considered as those under constant suction. For the same σ_{3n}, specimens show strain-hardening, shrinkage, and drum-shaped shear failure under low-s conditions and strain-softening, dilatancy, and oblique section splitting under high-s conditions. The failure deviator stress and cohesion of the compacted loess specimens increase with increasing s over the full s range (0–299.37 MPa). An equation to predict the shear strength of unsaturated loess over a wide s range is proposed. The intersection of the capillary water retention curve and adsorption water retention curve is set as a reference point (s_R), where capillary degree of saturation is applicable for $s \leq s_R$ and adsorption degree of saturation is added for $s > s_R$. The predicted and measured shear strengths of the compacted loess specimens are in good agreement.

Keywords: adsorption degree of saturation; capillary degree of saturation; prediction; shear strength; soil-water retention curve; unsaturated loess; wide suction range

1. Introduction

Loess is an inexpensive engineering material that is commonly used as a sub-base for roads after ground improvement via compaction. The subgrade loess project of National Highway G310 in Sanmenxia, Henan Province, China consists of embankments, bridges, and tunnels (Fig. 1). Loess is unsaturated under high-*s* conditions in arid and semi-arid areas owing to the low relative humidity, and tends to change in response to water storage or diversion. Geological hazards (e.g., sinkholes, landslides, mudflows) are prone to occur upon loess collapsibility under adverse weather conditions such as rainfall. Subgrade loess therefore poses numerous engineering problems (Hu *et al.* 2018, Chen *et al.* 2019, Wang *et al.* 2020, Pu *et al.* 2021). Suction is widely recognized to effectively improve the engineering properties of unsaturated soils (e.g., slope stability, strength, bearing capacity) (Leong and Abuel-Naga 2018, Abd *et al.* 2020). An understanding of the influence of suction on the hydromechanical behavior of unsaturated compacted loess is therefore required to resolve infrastructure problems.

Unsaturated loess undergoes hydraulic and mechanical changes under the influence of suction. Ma *et al.* (2017) showed that loess is sensitive to hydraulic wetting owing to its metastable and porous structure, and that the water retention behavior of loess differ from other soils. Previous studies have addressed the mutual coupling progress of water volume changes using soil-water retention curves (SWRCs) (Zhou *et al.* 2012, Jiang *et al.* 2016, Liang *et al.* 2018, Wu *et al.* 2019, Mu *et al.* 2020). The mechanical behavior of unsaturated loess is related to the suction (*s*) and net stress conditions. Zhang *et al.* (2020) carried out a series of triaxial tests on loess at *s* conditions of 50, 100 and 200 kPa, and showed an increase of stiffness and strength owing to *s* at a given net cell pressure (σ_{3n}). Loess under higher σ_{3n} was also shown to exhibit higher deviator stress at failure. Similar observations have been reported in studies of loess stress-strain characteristics (Li *et al.* 2014, Mei *et al.* 2016, Liang *et al.* 2016, Ng *et al.* 2020, Zhang *et al.* 2021). However, the *s* range of such tests has generally been limited to 0-500 kPa, whereas the hydromechanical behavior of unsaturated loess over a wider *s* range remains poorly constrained.

The control and measurement of *s* is the first critical step to build the core concept and theoretical basis of unsaturated soil research. Various tests have concentrated on the influence of *s* over a limited *s* range owing to air entry restrictions of the ceramic disk and other factors (Sun

*Corresponding author, Professor, Ph.D.
E-mail: zhangjunran@ncwu.edu.cn

ISSN: 2005-307X (Print), 2092-6219 (Online)

et al. 2010, Jiang *et al.* 2014, Zhang *et al.* 2020). The quick suction measurement technique using a chilled mirror dew point device performs well at high *s*, but measurements tend to be underestimated at low *s* (Bulut and Leong 2008). A wide *s* range can in fact be controlled using different methods. Gao *et al.* (2018) used the axis translation technique and vapor equilibrium technique to investigate the hydromechanical behavior of Pearl clay. Zhang *et al.* (2016, 2020) and Chen *et al.* (2020) used the same approach to analyze the hydromechanical behavior of other soils. On the basis of the above two methods, Sun *et al.* (2016) and Cai *et al.* (2020) added the filter paper method to measure the hydromechanical behavior of Guilin lateritic clay. However, only a small number of studies have incorporated the dew point method for SWRC measurements over a wide *s* range (Rahardjo *et al.* 2019, Satyanaga *et al.* 2019). Further research is therefore necessary to more effectively apply these methods. Suction control over a wide *s* range using multiple techniques remains an active area of study.

The strength prediction equation is a good approximation for unsaturated shear strength in the absence of experimental data. The main difference is the expression for the unsaturated effective stress coefficient χ (Bishop *et al.* 1959, Guan *et al.* 2010). The degree of saturation (S_r) obtained from SWRCs has been widely embedded within strength predictions for unsaturated soils considering its close correlation with shear strength. This leads to an appreciable overestimation of shear strength under high-*s* conditions. Other parameters were substituted for subsequent studies: the effective degree of saturation that deducting the residual degree of saturation (S_{re}) or microscopic degree of saturation (S_{rm}). However, the unsaturated strength enhancement term equals zero if *s* is equal to or greater than the residual *s*, thus strength predictions remain difficult in the dry state (Vanapalli *et al.* 1996, Oberg and Sallfors 1997, Alonso *et al.* 2010, Sheng *et al.* 2011, Zhou and Sheng 2015). According to different nonlinear states of strength varying with suction, the influence of soil type should be considered to predict the shear strength of soil. Gao *et al.* (2020) proposed a shear strength equation of unsaturated sands or silts based on the maximum skeleton stress, but less effort has been put forward to find a suitable equation for loess. A suction stress characteristic framework has been proposed to predict shear strength using the concepts of capillary and adsorptive mechanisms (Greco and Gargano 2015, Lu 2016, Maleksaeedi and Nuth 2019). Previous studies of unsaturated soils have shown that shear strength predictions are significantly improved using capillary degree of saturation under moderate *s* (Zhou *et al.* 2017, Xu *et al.* 2018), but the more prominent contribution of adsorption over a very high *s* range has been ignored. An approach to describe the role of capillary water and adsorbed water over a wide *s* range also remains unclear (Ng *et al.* 2017). Further research is therefore needed to establish a reasonable prediction equation of loess shear strength.

To address these problems, this paper investigates the hydromechanical behavior and shear strength prediction of unsaturated loess over a wide *s* range of 0 to 299.37 MPa. The water retention behavior of loess was investigated using the axis translation technique, vapor equilibrium technique, and chilled mirror dew point technique. The mechanical behavior of compacted loess was analyzed using a geotechnical digital system (GDS) triaxial apparatus over the same *s* range under σ_{3n} of 100, 200 and 300 kPa. A modified shear strength prediction equation is proposed for unsaturated loess over the investigated *s* range.

2. Test material

Intact loess was collected from a depth of 4–5 m below the surface of Dongshang Village, 1.2 km from the southern bank of the Yellow River in Sanmenxia, China. The particle size distribution (Fig. 2) indicates that the loess is composed of silt (77.24%), clay (24.9%), and sand (8.66%). The coefficient of curvature C_c and coefficient of uniformity C_u are 2.57 and 12.43, respectively. The other physical parameters are illustrated in Table 1. The loess is considered silty clay with low plasticity.

Mineral components within the loess samples were measured using X-ray diffraction, as listed in Table 2. The loess consists of 81% non-clay minerals (quartz, albite, microcline, calcite, amphibole) and 19% clay minerals (illite, montmorillonite, clinochlore, kaolinite), which indicates that non-clay minerals play a leading role in the loess properties.

Fig. 3 presents the results of mercury intrusion porosimetry (MIP) tests on the compacted loess with a

Fig. 1 Embankment, bridge, tunnel, and route map of National Highway G310

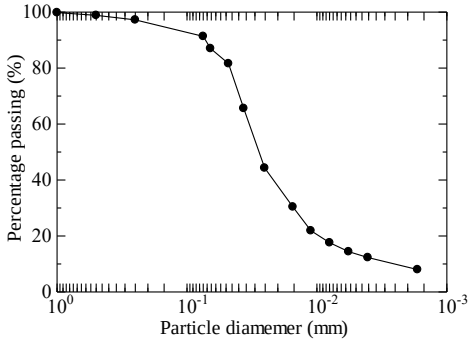

Fig. 2 Particle-size distribution of loess

Table 1 Physical parameters of loess

Physical parameters	Values
Liquid limit, w_L (%)	26.92
Plastic limit, w_P (%)	18.06
Plasticity index, I_P	12.79
Specific gravity of the solid, G_s	2.70
Natural water content, w_0 (%)	5.10
Natural dry weight, ρ_{d0} (g/cm^3)	1.33
Optimal water content, w_{opt} (%)	17.70
Maximum dry density, ρ_{dmax} (g/cm^3)	1.74

Table 2 Mineralogical composition of loess

Classification	Mineral	Content (%)
No-clay mineral	Quartz	52
	Albite	13
	Calcite	9
	Microcline	5
	Amphibole	3
Clay mineral	Illite	13
	Montmorillonite	3
	Clinochlore	2
	Kaolinite	1

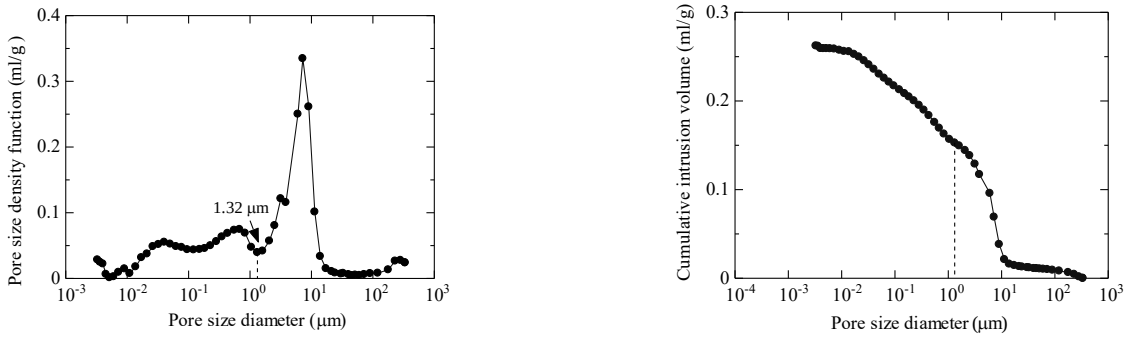

(a) Pore size density function (b) Cumulative intrusion curve

Fig. 3 MIP test results on loess

water content of 12.5% and dry density of 1.5 g/cm^3. The pore size density function illustrated in Fig. 3(a) shows that the maximum pore diameter (microscopic pores) in the aggregates was approximately 1.32 μm (Zhang *et al.* 2016, Sun *et al.* 2019). Fig. 3(b) shows that the microscopic volume of loess with grains smaller than 1.32 μm accounts for approximately 41.7% of the total volume. This implies that S_{rm} = 41.7 %.

3. Test apparatus and experimental techniques

3.1 Pressure plate device

A pressure plate device was used to measure the SWRCs of loess under low-*s* conditions based on the axis translation technique (ATT), as shown in Fig. 4. The *s* range of the apparatus is 0–0.5 MPa owing to limitations of the ceramic disk (Zhang *et al.* 2020, Jiang *et al.* 2020).

Fig. 4 The pressure plate device

3.2 Vapor equilibrium technique (VET)

The triaxial test specimens were placed in a sealed

Fig. 5 The Water Potential 4C

desiccator containing a specific saturated salt solution, as shown in Fig. 5. Two months were required to achieve suction balance. Suction was considered to have reached equilibrium when the change in specimen quality was less than 0.02 g over a week. The saturated saline solutions and their corresponding relative humidity and s values at 25 °C are summarized in Table 3, which are from Greenspan (1977). The total s is calculated using Kelvin's law (Zhang *et al.* 2020):

$$\psi = -\frac{\rho_w RT}{\omega_v} \ln(\mathrm{RH}) \quad (1)$$

where ψ is the total suction (kPa), ρ_w is the water density (g/cm^3), R is the universal gas constant (8.31432 J/mol·K), T is the absolute temperature, ω_v is the molecular weight of water vapor, which is assumed to be 18.016 g/mol, and RH is the relative humidity (%).

3.3 Water potential 4C (WP4C)

The WP4C (shown Fig. 5) uses the chilled mirror dew point technique to measure the water potential of the specimen. The principle is to measure the soil water potential by determining the RH of the air above the specimen in a sealed chamber. The relationship between ψ and RH can also be expressed by Kelvin's equation. The accuracy of the WP4C method is in the range of 0.1 to 300 MPa and can obtain an s value within 5-10 min.

Considering the influence of temperature and environment on relative humidity, the device must first be calibrated using a saturated salt solution. The temperature was maintained at 25°C using air conditioning. A standard 0.5 M KCl solution was poured into the specimen cup and placed in the chamber. The calibration was completed when s reached within ±0.05 of 2.22 MPa; otherwise, an additional step was applied to correct the s value. Eight other saturated saline solutions were added and the data were read for further calibration. A comparison of the results in Table 3 shows that the reference s values obtained from Greenspan (1977) are consistent with the values measured in the calibration test, which supports that the WP4C method is applicable for measuring high s.

3.4 GDS triaxial apparatus

The unsaturated soil triaxial apparatus is produced by GDS company, UK. This apparatus also controls the s through ATT (Gao *et al.* 2018).

Table 3 Saturated saline solution and the corresponding suction (25°C)

Saturated saline solution	Relative humidity (%)	Reference suction value (MPa)	Measured suction value (MPa)
$LiCl{\cdot}H_2O$	11.3	299.37	299.14
$MgCl_2{\cdot}6H_2O$	32.8	153.06	153.88
K_2CO_3	43.2	115.24	115.27
NaBr	57.6	75.74	76.11
KI	68.9	51.15	51.26
NaCl	75.3	38.95	39.00
KCl	84.2	23.61	23.61
K_2SO_4	97.3	3.76	3.76

4. Testing program and suction path

4.1 Water retention behavior tests

Different techniques were combined to analyze the water retention behavior of loess over a wide s range. Specimens under low s (0-0.4 MPa) were balanced using the pressure plate device and GDS triaxial apparatus, and specimens under high s (3.76-299.37 MPa) were controlled by the VET using four saturated saline solutions. The s path for the pressure plate method is shown in Table 4. Water retention behavior tests of loess powder and compacted loess of three dry densities were also carried out using the WP4C.

The initial water content for the pressure plate method was approximately 12.5% and the dry density was approximately 1.5 g/cm^3. The specimens (diameter = 61.8 mm, height = 20 mm) were placed in the device after saturation. For the VET, the specimens (diameter = 76 mm, height = 38 mm) had the same initial water content and dry density as those tested using the pressure plate method. In the WP4C tests, the target water contents of loess were 2.5%, 5%, 7.5%, 10%, 12.5%, 15%, and 17.5%. Small specimens (diameter = 33 mm, height = 7 mm) with different water contents were prepared with dry densities of 1.3, 1.4, and 1.5 g/cm^3. The specimens used in the WP4C are shown in Fig. 6.

4.2 GDS triaxial shear tests

A series of GDS unsaturated triaxial shear tests were conducted on the compacted loess over a wide s range and σ_{3n} of 100, 200 and 300 kPa. The specimen size, initial water content, and initial dry density were the same as those tested using the VET. Fig. 7 shows the stress and s paths for the triaxial tests under different σ_{3n}. The q in Fig. 7 represents the deviator stress. The σ_{3n} was determined by the difference between the cell pressure and pore air pressure (u_a). The tests CL 1-5 in Fig. 7(a) were conducted under low s (0, 50, 100, 200, 300 kPa), which was achieved

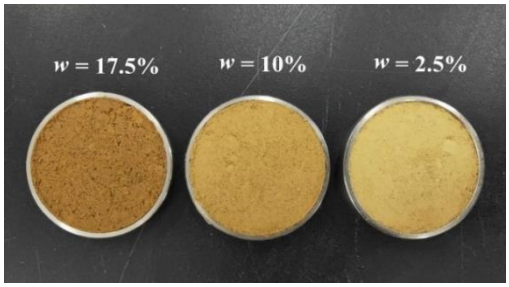

Fig. 6 Loess specimens with different water contents

Table 4 Suction design in the soil-water retention tests

Path type	Suction path
Drying	0 kPa→5 kPa→10 kPa→20 kPa→ 40 kPa→ 60 kPa→80 kPa→100 kPa→ 120 kPa→240 kPa→400 kPa

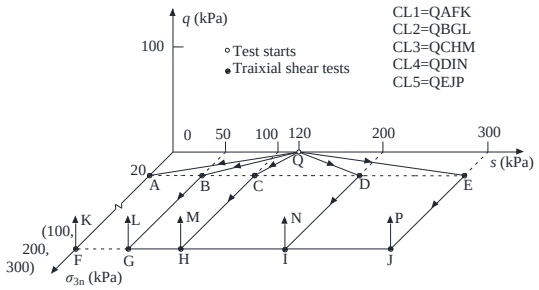

(a) Maximum suction was achieved by ATT

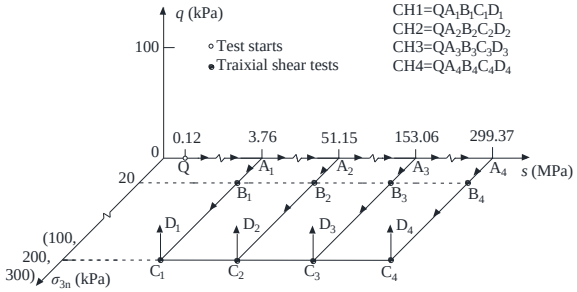

(b) Maximum suction was achieved by VET

Fig. 7 Stress and suction paths for triaxial tests under different net cell pressures

Table 5 The state of triaxial specimen at different stages

Test no.	Molding state			Before triaxial shearing			*s* (MPa)	Stress path	σ_{3n} (kPa)
	w_0	S_{r0} (%)	e_0	w	S_r (%)	e			
1	13.48	44.93	0.81	26.63	99.86	0.72	0.00	CL1	
2	12.50	42.72	0.79	19.98	77.07	0.70	0.05	CL2	
3	12.68	42.27	0.81	14.19	55.53	0.69	0.10	CL3	
4	12.36	43.34	0.77	10.65	45.64	0.63	0.20	CL4	
5	12.59	43.03	0.79	9.19	40.02	0.62	0.30	CL5	100
6	12.64	42.13	0.81	5.68	25.14	0.61	3.76	CH1	
7	13.21	42.97	0.83	3.13	14.09	0.60	51.15	CH2	
8	12.39	42.35	0.79	0.65	2.83	0.62	153.06	CH3	
9	12.05	41.18	0.79	0.43	1.90	0.61	299.37	CH4	
10	12.89	42.97	0.81	25.59	97.31	0.71	0.00	CL1	
11	12.67	42.76	0.80	19.03	74.47	0.69	0.05	CL2	
12	11.47	39.70	0.78	13.72	55.29	0.67	0.10	CL3	
13	12.65	45.54	0.75	10.99	47.10	0.63	0.20	CL4	
14	12.21	41.73	0.79	9.77	42.55	0.62	0.30	CL5	200
15	12.25	40.83	0.81	5.59	24.34	0.62	3.76	CH1	
16	12.42	41.40	0.81	3.62	16.02	0.61	51.15	CH2	
17	12.73	42.96	0.80	0.78	3.45	0.61	153.06	CH3	
18	12.54	41.80	0.81	0.37	1.67	0.60	299.37	CH4	
19	12.51	41.70	0.81	25.51	98.40	0.70	0.00	CL1	
20	12.43	42.48	0.79	18.95	74.15	0.69	0.05	CL2	300
21	11.90	41.19	0.78	13.93	54.51	0.69	0.10	CL3	

Table 5 Continued

Test no.	Molding state			Before triaxial shearing			s (MPa)	Stress path	σ_{3n} (kPa)
	w_0	S_{r0} (%)	e_0	w	S_r (%)	e			
22	12.39	42.35	0.79	10.22	43.80	0.63	0.20	CL4	300
23	12.64	42.66	0.80	9.50	41.35	0.62	0.30	CL5	
24	12.41	41.37	0.81	5.03	21.90	0.62	3.76	CH1	
25	12.59	42.49	0.80	3.36	14.63	0.62	51.15	CH2	
26	12.49	43.80	0.77	1.05	4.57	0.62	153.06	CH3	
27	12.51	42.76	0.79	0.36	1.59	0.61	299.37	CH4	

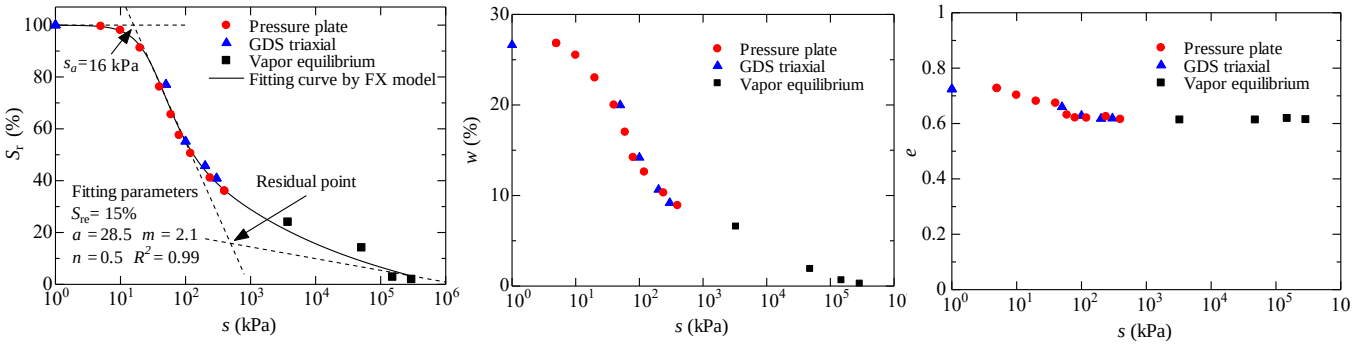

(a) S_r-s (b) w-s (c) e-s

Fig. 8 Measured SWRCs of loess

using the ATT. The tests CH 1-5 in Fig. 7(b) were conducted under high s (3.76, 51.15, 153.06, 299.37 MPa), which was achieved using the VET. Specimen consolidation and drainage were considered stable when the rates of volume change and drainage were less than 0.005 cm^3/h. To ensure the uniformity of the pore water pressure distribution in the specimen, the shear rate was set to 0.0027 mm/min and the maximum shear strain reached 15% over approximately 3 days. The initial s of the specimens measured using the ATT on the triaxial apparatus was approximately 120 kPa (Q in Fig. 7). Table 5 summarizes the state of the triaxial specimens at different stages.

5. Results and discussion

Fig. 8 shows the loess SWRCs obtained using the ATT and VET under a σ_{3n} of 100 kPa. The FX model proposed by Fredlund and Xing (1994) was used to more accurately fit the loess results, according to:

$$S_r = \frac{[1 - \ln(1 + \frac{s}{s_{re}}) / \ln(1 + \frac{10^6}{s_{re}})]}{[\ln(e + (\frac{s}{a})^n)]^m} \quad (2)$$

where s_{re} is the residual suction, and a, n and m are fitting parameters equal 28.5, 0.5 and 2.1 for loess, respectively.

The relationship between the S_r and s is shown in Fig. 8(a). The goodness of fit (R^2 = 0.99) verifies the accuracy and validity of the available data using the FX model. The smooth curve indicates that the air entry value (s_a) and S_{re} can be estimated as 16 kPa and 15%, respectively.

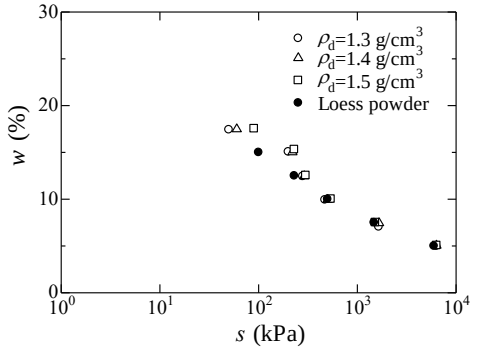

Fig. 9 SWRCs of compacted loess and loess powder obtained by the WP4C

Fig. 8(b) shows the relationship between the matric s and water content. Water content generally decreases with increasing s; initially decreasing strongly and then following a linearly decreasing trend. The specimens under low s were easily dehydrated under the action of capillary water, and the water holding capacity was weak. Fig. 8(c) shows the small influence of s on the void ratio. The void ratio is sensitive to s mainly in the range of s < 80 kPa, which reflects that s within this range has the most significant compression effect on soil pores.

The SWRCs of the compacted loess with different dry densities and loess powder obtained by WP4C are shown in Fig. 9. The relationship between the compacted loess with different dry densities and loess powder is nearly the same for s > 0.5 MPa. This provides strong evidence for the undrained triaxial test is equal to those under constant suction under high s. Gao *et al.* (2018, 2021) and Zhang *et al.* (2020) obtained the same results for other soils.

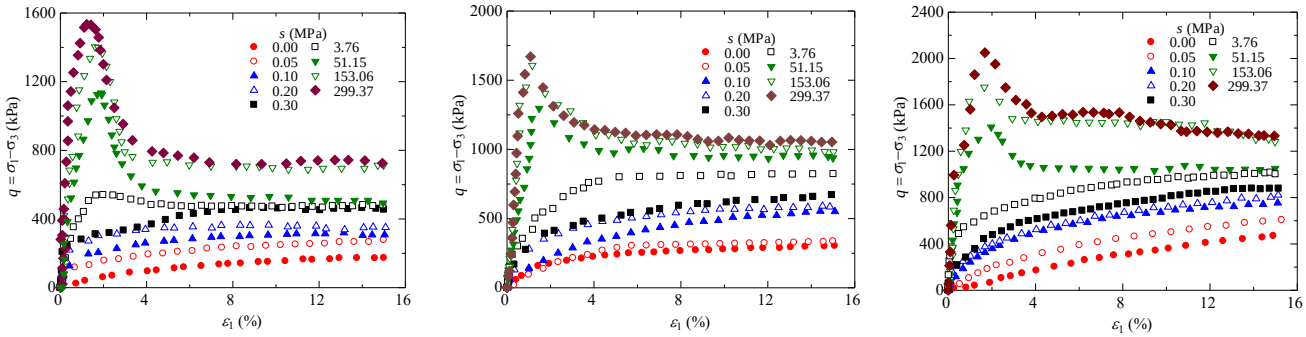

(a) σ_{3n} = 100 kPa (b) σ_{3n} = 200 kPa (c) σ_{3n} = 300 kPa

Fig. 10 The relationship between deviator stress and axial strain

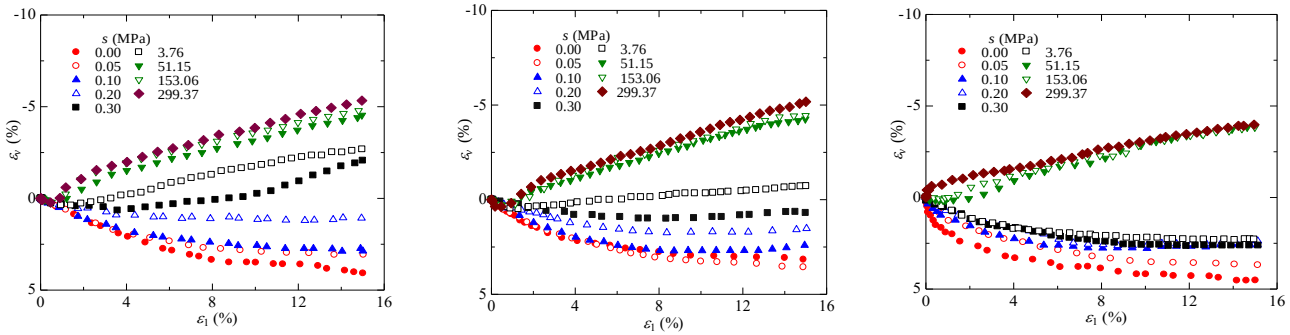

(a) σ_{3n} = 100 kPa (b) σ_{3n} = 200 kPa (c) σ_{3n} = 300 kPa

Fig. 11 Relationship between volumetric strain and axial strain

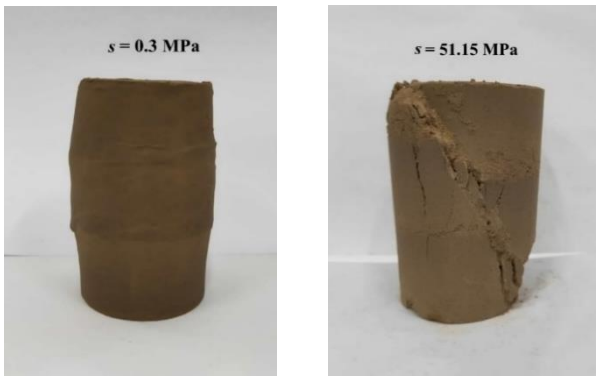

(a) s = 0.3 MPa (b) s= 51.15 MPa

Fig. 12 The shape of unsaturated loess after shearing under different suctions

5.2 Mechanical behavior

Fig. 10 depicts the curves of q versus axial strain (ε_1) over a wide range of s conditions and σ_{3n} of 100, 200 and 300 kPa from the triaxial shear tests. The stress-strain curves under low s show a strain-hardening behavior: q increases with increasing ε_1 and then stabilizes. The stress-strain curve moves upward gradually with increasing s. As s increased to a high value (called critical s), q reaches the peak shear strength, sharply decreases, and then stabilizes, demonstrating strain-softening behavior at different degrees. A comparison of the three different σ_{3n} curves shows that the critical s of loess also tends to increase with increasing σ_{3n}. The critical s is approximately 3.76 MPa under a σ_{3n} of 100 kPa and then increases to approximately 51.15 MPa when the σ_{3n} is 200 and 300 kPa. Under the same s condition, the stress-strain relationship differs depending on the σ_{3n}. For s = 3.76 MPa, strain softening occurs at low σ_{3n} (100 kPa). Under intermediate σ_{3n} (200 kPa), the stress-strain relationship becomes an ideal elastic-plastic type, and strain hardening occurs when the σ_{3n} is 300 kPa. The slope of the stress-strain curve in the initial linear segment, termed the elastic modulus, increases with increasing s (Zhang *et al.* 2020). The axial strain corresponding to the peak shear strength also decreases with increasing s. Larger s is therefore associated with an earlier deviator stress peak and earlier failure.

Fig. 11 shows the relationship between volumetric strain (ε_v) and ε_1 during shearing, in which negative ε_v values indicate dilative volume change. The results show that the specimens exhibit shearing shrinkage under low-s conditions and expansion under high-s conditions. This is mainly because of the loss of water and reduction of the void ratio during the transition from low to high s. The specimen deformation characteristics are similar to those of the over-consolidated unsaturated soil in the shear tests. For the same imposed s conditions, larger σ_{3n} are associated with more notable shear contraction (except for the saturated specimen). As an example, the specimen with s = 3.76 MPa undergoes dilation, weak shear contraction, and shear contraction under σ_{3n} of 100, 200 and 300 kPa, respectively.

Compacted loess with s values of 0.3 and 51.15 MPa under a σ_{3n} of 100 kPa were selected as representative specimens to analyze the specimen shape after shearing.

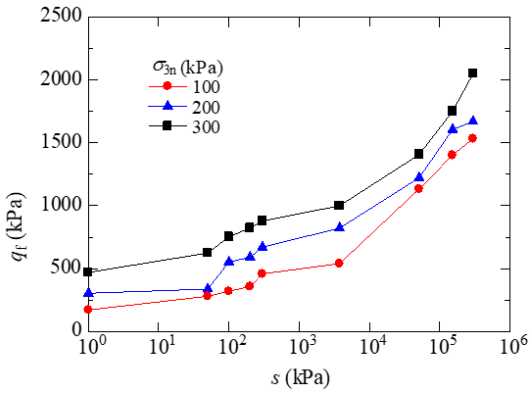

Fig. 13 Relationship between failure deviator stress and suction

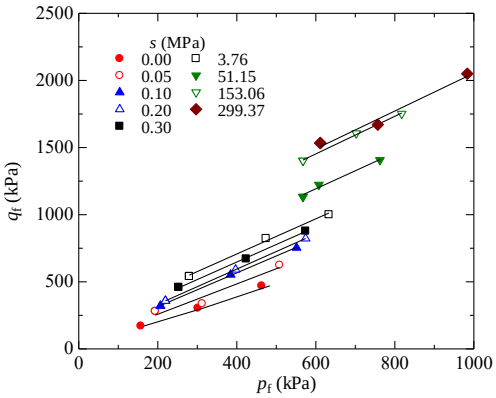

Fig. 14 Relationship between failure deviator stress and mean net stress

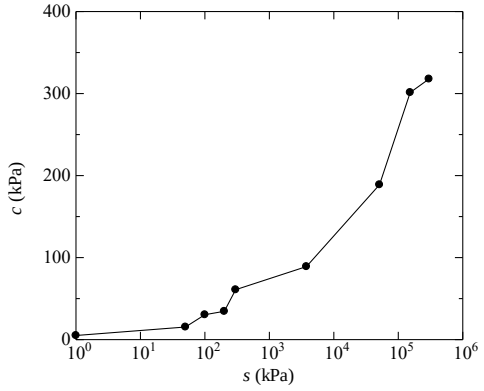

Fig. 15 Relationship between cohesion and suction

Fig. 12 shows that the compacted specimen demonstrates a cylindrical drum-type after the triaxial shear test under low s (0.3 MPa). The specimen shows a visible shear band in the high-s case (51.15 MPa), which is called the failure form of oblique section splitting. The characteristics of brittle failure and an apparent shear zone occur after shear failure. The different types of shear morphology under high s are related to the appearance of strain softening and dilatancy.

The q corresponding to the maximum ε_1 of 15% or the peak point is taken as the failure deviator stress (q_f) for the strain-hardening or strain-softening curves, respectively. The tests result of q_f varying with s under the different σ_{3n} are shown in Fig. 13. Under the same σ_{3n}, q_f increases with increasing s and does not show a stable or peak value. Specimens under higher σ_{3n} conditions show higher shear strengths.

Fig. 14 presents the critical state curve of q_f and net mean stress ($p_f = q_f/3+\sigma_{3n}$) at failure and residual of loess over the full s range. The shear parameters obtained from

Table 6 Shear parameters of loess

s (MPa)	σ_{3n} (kPa)	q_f (kPa)	p_f (kPa)	ξ (kPa)	M_f	c (kPa)	φ (°)
0.00	100	171.28	157.09	1.77	1.04	5.04	25.34
	200	304.31	301.44				
	300	470.20	463.07				
0.05	100	280.79	193.60	32.17	1.13	15.39	28.39
	200	337.44	312.48				
	300	624.69	508.23				
0.10	100	320.10	206.70	62.85	1.26	30.42	31.36
	200	553.05	384.35				
	300	753.75	551.25				
0.20	100	358.03	219.34	70.96	1.31	34.54	32.50
	200	590.85	396.94				
	300	822.65	574.22				
0.30	100	458.62	252.87	125.19	1.31	60.90	32.41
	200	670.92	423.64				
	300	878.50	574.22				
3.76	100	480.25	477.83	183.07	1.31	89.07	32.45
	200	822.59	474.20				
	300	1000.04	633.33				
51.15	100	1133.50	567.49	386.48	1.34	188.89	33.30
	200	1223.00	607.67				
	300	1387.00	762.33				
153.06	100	1402.47	567.49	611.73	1.40	301.29	34.62
	200	1506.40	702.13				
	300	1551.81	817.27				
299.37	100	1533.94	611.31	644.47	1.41	317.79	34.81
	200	1670.40	756.80				
	300	2050.01	983.33				

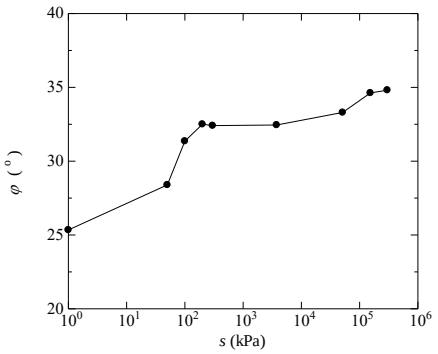

Fig. 16 Relationship between internal friction angle an suction

the triaxial tests are listed in Table 6, where ξ and M_f are the intercept and slope of the line in the p_f-q_f plane, respectively. The cohesion ($c = \xi(3\text{-}\sin\varphi)/(6\cos\varphi)$) and internal friction angle ($\varphi = \arcsin(3M_f/6+M_f)$) can also be calculated by M_f and ξ. As shown in Figs. 15 and16, the c of compacted loess exhibited increased trends with the increase of s, and φ also increases slightly. The change of φ mainly occurs for s < 200 kPa.

6. Shear strength prediction of loess over a wide suction range

The shear strength of unsaturated soil consists of three parts: effective cohesion (c'); net stress; and suction. The strength prediction equation proposed by Bishop (1959) based on the single stress variable theory is expressed as:

$$\tau = c' + (\sigma - u_a)\tan\varphi' + \chi s\tan\varphi' \tag{3}$$

$$q = c'\frac{6\cos\varphi'}{3-\cos\varphi'} + M(\bar{p} + \chi s) \tag{4}$$

where σ is the total stress, φ' is the effective internal friction angle, $\bar{p} = [(\sigma_1+2\sigma_3)/3]\text{-}u_a$ is the net mean stress, $M = 6\sin\varphi'/(3\text{-}\sin\varphi')$ represents the slope of the failure envelope on the space of $\bar{p}$–q plane. From the saturated shear test, c' = 5 kPa and φ' = 25.34°.

Based on the extended spatially mobilized plane failure criterion (Sun *et al.* 2000, Lu 2016), the suction stress $\sigma_0(s)$ that considers the influence of s on unsaturated soil is embedded in the failure criterion:

$$\tau = c' + (\sigma - u_a)\tan\varphi' - \sigma_0(s)\tan\varphi' \tag{5}$$

$$q = c'\frac{6\cos\varphi'}{3-\cos\varphi'} + M(\bar{p} - \sigma_0(s)) \tag{6}$$

where

$$\sigma_0(s) = -\chi s \tag{7}$$

With the development of shear strength prediction research, numerous models have been proposed by several investigators. Table 7 summarizes the strength prediction equations of unsaturated soils commonly found in previous literatures. The difference between these equations is mainly reflected in the effective stress parameter χ.

Eq. (8) is a further description of the equation proposed by Zhou *et al.* (2016). The S_r is divided into two parts: capillary degree of saturation (S_r^{cap}) and adsorption degree of saturation (S_r^{ads}). The SWRC is correspondingly superimposed by the capillary water retention curve (CWRC) and adsorption water retention curve (AWRC). The capillary includes the curvature of the water-air interface and negative pore water pressure, and the adsorption is mainly related to the adsorbed water and minerals on the surface of the soil particles. The capillary water function gradually weakens as the soil varies from saturated to unsaturated conditions (Liu *et al.* 2020). In the dry state, capillary water is entirely vaporized and adsorbed water plays a dominant role (Zhang and Lu 2021). According to the shear strength criterion proposed by Zhou *et al.* (2016), only the capillary component of degree of saturation is applied to the shear strength prediction and its contribution to the shear strength of unsaturated soil is directly related to capillary water rather than adsorbed water.

Table 7 The equations for shear-strength prediction of unsaturated soils

Authors	χ
Vanapalli *et al.* (1996)	$(S_r\text{-}S_{re})/(1\text{-}S_{re})$
Oberg and Sallfors (1997)	S_r
Alonso *et al.* (2010)	$(S_r\text{-}S_{rm})/(1\text{-}S_{rm})$
Zhou *et al.* (2016)	$S_r^{cap} = \dfrac{C(\varphi) - \alpha C(\varphi)A(\varphi)}{1 - \alpha C(\varphi)A(\varphi)}$ $S_r^{ads} = \dfrac{\alpha A(\varphi) - \alpha C(\varphi)A(\varphi)}{1 - \alpha C(\varphi)A(\varphi)}$ $C(\varphi) = \dfrac{1}{2}erfc\left(\dfrac{\ln(\varphi/\varphi_m)}{\sqrt{2}\xi}\right)$ $A(\varphi) = 1 - \ln(\varphi/\varphi_d)$ Where the ξ, φ_m, α are derived from the SWRC

$$S_r = S_r^{cap} + S_r^{ads} = \frac{C(\varphi) + \alpha A(\varphi) - 2\alpha C(\varphi)A(\varphi)}{1 - \alpha C(\varphi)A(\varphi)} \tag{8}$$

Gao *et al.* (2020) divided soil into three types based on the variation of shear strength with increasing s: (1) "peak type", in which the strength gradually increases to a peak value and then sharply decreases to stabilize; (2) "stable type", in which the strength gradually increases to a constant or maximum value and then slightly decreases; and (3) "growth type", in which the strength continually increases. On the basis of the maximum average skeleton stress (Sun *et al.* 2014, Zhao *et al.* 2016) that differentiates consolidation from over-consolidation (Eq. (9)), Gao *et al.* (2020) proposed a modified shear strength equation for peak and stable types (Eq. (10)) over a wide s range. Considering the absence of net stress using the pressure plate method and VET, the average skeleton stress $p' = \sigma_0(s) = -\chi s$. Similar to the relationship between q_f and s, the average skeleton stress consistently increases with increasing s, thus there is no maximum average skeleton stress in loess (called "growth type" soil). This equation only considers S_r^{cap} when calculating the shear strength of loess, which is essentially the same as the equation proposed by Zhou *et al.* (2016). In order to predict the shear strength of "growth type" soil, a correction parameter (η) is introduced into the equations proposed by Khalili and Khabbaz (1998) and Tekinsoy *et al.* (2004). It is worth noting that the parameters used in the two modified equations are precisely identical. The two modified prediction equations for the shear strength of "growth type"

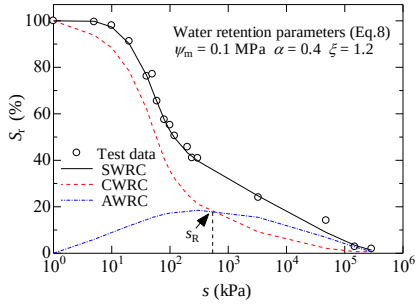

Fig. 17 Water retention behavior and model prediction results using Eq. (8)

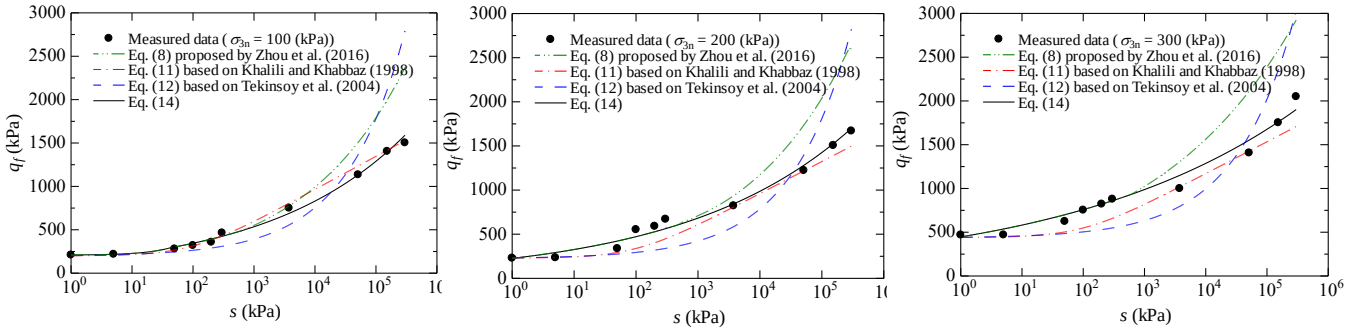

(a) σ_{3n} = 100 kPa (b) σ_{3n} = 200 kPa (c) σ_{3n} = 300 kPa

Fig. 18 Measured and predicted deviator stress for unsaturated Sanmenxia loess soils at failure

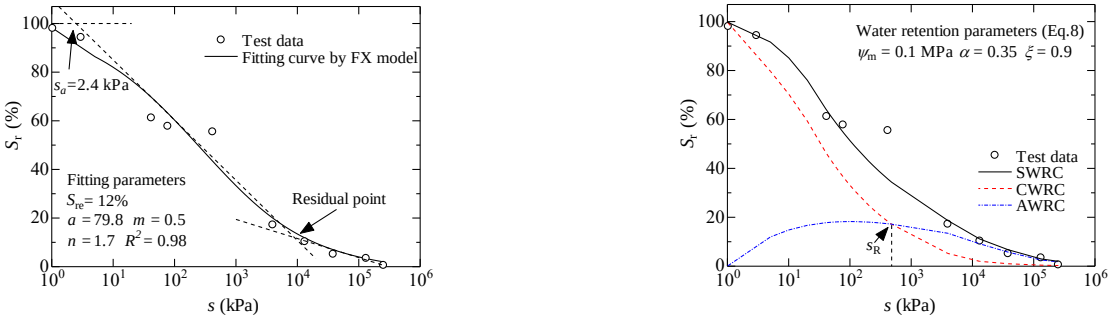

(a) SWRC predicted by the FX model (b) SWRC, CWRC, and AWRC predicted by Eq. (8)

Fig. 19 Measured water retention behavior of loess (data after Ng *et al.* 2020) and model simulations

soil are expressed as Eqs. (11) and (12), respectively.

$$\sigma'_{ij} = \sigma_{ij} - u_a\delta_{ij} - \sigma_0(s)\delta_{ij} \tag{9}$$

$$\begin{aligned} \tau &= c + (\sigma - u_a)\tan\varphi' + \chi s\tan\varphi', s \le s_{max} \\ \tau &= \tau_{max} + (\chi s - \chi_{max}s_{max})\tan\varphi_s, s > s_{max} \end{aligned} \tag{10}$$

$$\tau = c' + (\sigma - u_a)\tan\varphi' + s(\frac{s}{\eta s_a})^{-0.55}\tan\varphi' \tag{11}$$

$$\tau = c' + (\sigma - u_a)\tan\varphi' + (\eta s_a + P_{at})\ln(\frac{s + P_{at}}{P_{at}})\tan\varphi' \tag{12}$$

where σ'_{ij} is the average soil skeleton stress, σ_{ij} is the total stress tensor, δ_{ij} is Kronecker's delta, s_{max}, q_{max}, and χ_{max} are the parameters related to maximum average skeleton stress p'_{max}, P_{at} is atmospheric pressure (kPa).

Take the s corresponding to the intersection of the CWRC and AWRC as the reference point (s_R), χ in the two expressions in Eq. (10) proposed by Gao *et al.* (2020) are replaced by S_r^{cap} and S_r^{ads}, respectively. According to the "contribution factor" and "the link between unimodal pore size distribution and water storage mechanisms" proposed by Qiao *et al.* (2020), the maximum contribution of capillarity to the water retention is much higher than that of adsorption for loess when $s \le s_R$ (Fig. 3(a)). In the case of $s > s_R$, AWRC is the upper curve, the micropores or nanopores is considered to play a significant role in loess soil. The influence of absorbed water on shear strength cannot be ignored. Since both S_r^{cap} and S_r^{ads} should be considered in high s, the sution stress at the intersection is deducted based on the suction stress caused by S_r^{ads}. The modified prediction equation of unsaturated loess under a wide s range is given in Eq. (13), and the corresponding failure criterion under triaxial conditions is given in Eq. (14).

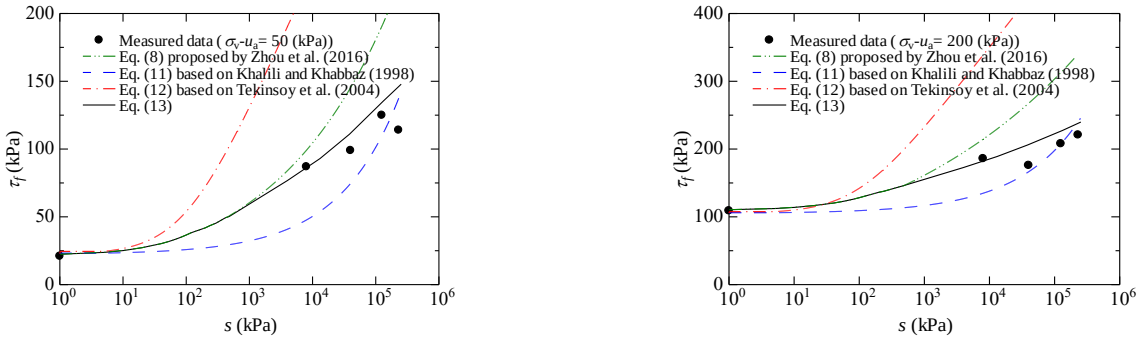

(a) σ_v-u_a = 50 kPa (b) σ_v-u_a = 200 kPa

Fig. 20 Loess shear strength (data after Ng *et al.* 2020) and model simulations

$$\begin{aligned}\tau &= c' + (\sigma - u_a)\tan\varphi' + S_r^{cap} s \tan\varphi', s \le s_R \\ \tau &= \tau_R + (S_r^{ads} s - S_{rR} s_R)\tan\varphi_R, s > s_R\end{aligned} \quad (13)$$

$$\begin{aligned}q &= c' \frac{6\cos\varphi'}{3-\cos\varphi'} + M(\bar{p} + S_r^{cap} s), s \le s_R \\ q &= q_R + M_R(S_r^{ads} s - S_{rR} s_R), s > s_R\end{aligned} \quad (14)$$

where τ_R, S_{rR}, φ_R, q_R, and M_R are the parameters corresponding to the intersection of the CWRC and AWRC.

For loess, the degree of saturation parameters S_{re} and S_{rm} are 15% and 41.7%, respectively. Additional parameters used in other equations to predict shear strength are listed in Table 8. The SWRC, CWRC, AWRC and water retention parameters of loess are shown in Fig. 17. The part fitting compared results of the shear strength at failure under the three different σ_{3n} are shown in Fig. 18. The equations fit differently for the intermediate and high s conditions. The unsaturated strength enhancement term equals zero when s is equal to or greater than the s corresponding to S_{re} or S_{rm}. Therefore, the shear strength calculation in the high s residual zone is invalid regardless of which form of effective degree of saturation is used. This is why shear strength cannot be correctly predicted at high s using the equations proposed by Vanapalli *et al.* (1996) and Alonso *et al.* (2010) (not shown in Fig. 18). The data in the high s range are overestimated when Eqs. (8) (proposed by Oberg and Sallfors (1997)) and (11) are used to predict the shear strength. The fitting results obtained using Eq. (12) perform well when σ_{3n} is 100 kPa, but the accuracy is insufficient when σ_{3n} is 200 or 300 kPa.

Since adsorption is more prominent at high s, S_r^{ads} is taken into account in the strength prediction of loess (Eq. (14)). The reference point s_R is 600 kPa for the loess, as shown in Fig. 17. The strength parameters M and M_R determined by fitting the test data are 1.2 and 0.2, respectively. A comparison of the measured and predicted strength data shown in Fig. 18 indicates that it is feasible to calculate the shear strength of unsaturated Sanmenxia loess over a wide s range.

7. Validation and comparison

Ng *et al.* (2020) conducted saturated and unsaturated s-controlled direct shear tests on compacted loess under different net vertical stresses. The soil consisted of 0.1% sand, 71.9% silt, and 28.0% clay particles, and was classified as low-plasticity clay, which is consistent with the Sanmenxia loess. Fig. 19(a) shows the SWRC of compacted loess predicted by the FX model where S_{re} = 12%, s_a = 2.4 kPa, a = 79.8, n = 1.7 and m = 0.5. Fig. 19(b) shows the SWRC, CWRC, and AWRC obtained using Eq. (8). The reference point s_R = 480 kPa, the effective friction angle is 27.7°, and the effective cohesion is considered to be zero from saturated shear tests. The strength parameter φ_R is 24.0°. The loess shear strength was measured at five s values (0, 8, 40, 125 and 230 MPa). Fig. 20 shows the measured and predicted loess shear strengths at different net vertical stresses (σ_v-u_a = 50 and 200 kPa). Eqs. (8) and (11)–(13) are used to predict the shear strength of compacted loess. The correction parameter η in Eqs. (11) and (12) is 0.4. The prediction using Eq. (11) leads to an underestimation in the intermediate s range, and Eqs. (8) and (11) overestimate the shear strength in the second transition zone and residual zone. The criterion that accounts for capillary and adsorptive processes (Eq. (13)) produces the best predictions over the entire s range.

Table 8 Additional parameters in the shear-strength equations for loess

Numbers	Additional parameters
8	ξ =1.2, φ_m = 0.1 MPa, α = 0.4
10	$\chi = S_r^{cap}$, no s_{max}
11	s_a = 16 kPa, η = 2
12	P_{at} = 100 kPa, η = 2
13	s_R = 600 kPa

8. Conclusions

In order to study the hydromechanical behavior of unsaturated loess under a large s range, the SWRC tests using multiple techniques and unsaturated triaxial shear tests under the constant σ_{3n} of 100, 200 and 300 kPa were carried out in this study. The main results are summarized as follows.

- The water content and degree of saturation of loess

decrease continuously with the increase of s until reaching a stable value at zero, and the variation range of the void ratio is small. Specimens under high net confining pressure generally show higher shear strength and shrinkage. When the s is greater than 0.5 MPa, the curves of gravimetric water content versus s are coincident for different initial dry densities measured using the chilled mirror dew point technique. This indicates that the undrained triaxial tests are equal to those under constant s.

- Specimens under low s show strain-hardening and shear contraction, whereas strain-softening and shear dilation occur in the high s range. The shear strain corresponding to the peak strength decreases with increasing s, and the loess shear zone is fully developed.
- Over the wide s range investigated here, increased s consistently leads to higher failure deviator stress and cohesion. The internal friction angle mainly increases for s < 200 kPa. Loess can be classified as "growth type" soil according to the variation of strength with s.
- An improved equation to predict loess shear strength is proposed that considers different capillary and adsorption mechanisms. By setting the intersection of the capillary water retention curve and adsorbed water retention curve (s_R) as a reference point, capillary degree of saturation is used for $s \leq s_R$ and adsorption degree of saturation is used for $s > s_R$. The prediction results match well with the measured values, which indicates that this new strength criterion is feasible for loess, especially at high s.

Acknowledgments

This study is financially supported by the National Natural Science Foundation of China (Grant No. 41602295), the Foundation for University Key Teacher by the Ministry of Education of Henan Province (Grant No. 2020GGJS-094), the Key Scientific Research Projects of Colleges and Universities in Henan Province (Grant No. 21A410002), the Natural Science Foundation of Guangxi (Grant No. 2019GXNSFAA245025), and the Doctoral Student Innovation Foundation of NCWU.

References

Abd, I.A., Fattah, M.Y. and Mekkiyah, H. (2020), "Relationship between the Matric Suction and the Shear Strength in Unsaturated Soil", *Case Stud. Construct. Mater.*, **13**, e00441. https://doi.org/10.1016/j.cscm.2020.e00441.

Alonso, E.E., Pereira, J.M., Vaunat, J. and Olivella, S. (2010), "A microstructurally based effective stress for unsaturated soils", *Geotechnique*, **60**(12), 913-925. https://doi.org/10.1680/geot.8.P.002.

Bishop, A.W. (1959), "The principle of effective stress", *Teknisk Ukeblad*, **106**(39), 859-863.

Bulut, R. and Leong, E.C. (2008), "Indirect measurement of suction", *Geotech. Geol. Eng.*, **26**(6), 633-644. https://doi.org/10.1007/s10706-008-9197-0.

Cai, G., Zhou, A.N., Liu, Y., Xu, R.Z. and Zhao, C.G. (2020), "Soil water retention behavior and microstructure evolution of lateritic soil in the suction range of 0-286.7 MPa", *Acta Geotechnica*, **15**, 3327-3341. https://doi.org/10.1007/s11440-020-01011-w.

Chen, B., Ding, X.H., Gao, Y., Sun, D.A. and Yu, H.H. (2020), "Hydro-mechanical behavior of compacted silt over a wide suction range", *Geomech. Eng.*, **22**(3), 237-244. https://doi.org/10.12989/gae.2020.22.3.237.

Chen, S., Ma, W. and Li, G. (2019), "Study on the mesostructural evolution mechanism of compacted loess subjected to various weathering actions", *Cold Reg. Sci. Technol.*, **167**, 102846. https://doi.org/10.1016/j.coldregions.2019.102846.

Fredlund, D.G. and Xing A.Q. (1994), "Equations for soil–water characteristic curve", *Can. Geotech. J.*, **31**(4), 521-532. https://doi.org/10.1139/t94-061.

Gao, Y., Sun, D.A., Zhou, A.N. and Li, J. (2020), "Predicting shear strength of unsaturated soils over wide suction range", *Int. J. Geomech.*, **20**(2), 04019175. https://doi.org/10.1061/(ASCE)GM.1943-5622.0001555.

Gao, Y., Sun, D.A., Zhu, Z.C. and Xu, Y.F. (2018), "Hydromechanical behavior of unsaturated soil with different initial densities over a wide suction range", *Acta Geotechnica*, **14**(2), 417-428. https://doi.org/10.1007/s11440-018-0662-5.

Gao, Y., Li, Z., Sun, D. A. and Yu, H.H. (2021), "A simple method for predicting the hydraulic properties of unsaturated soils with different void ratios", *Soil Till. Res.*, **209**(3), 104913. https://doi.org/10.1016/j.still.2020.104913.

Greco, R. and Gargano, R. (2015), "A novel equation for determining the suction stress of unsaturated soils from the water retention curvebased on wetted surface area in pores", *Water Resour. Res.*, **51**(8), 6143-6155. https://doi.org/10.1002/2014WR016541.

Greenspan, L. (1977), "Humidity fixed points of binary saturated aqueous solutions", *J. Res. Nat. Bureau Standards A Phys. Chem.*, **81**(1), 89-96. https://doi.org/10.6028/jres.081A.011.

Guan, G.S., Rahardjo, H. and Choon, L.E. (2010), "Shear strength equations for unsaturated soil under drying and wetting", *J. Geotech. Geoenviron. Eng.*, **136**(4), 594-606. https://doi.org/10.1061/(ASCE)GT.1943-5606.0000261.

Hu, C.M., Wang, X.Y., Mei, Y., Yuan, Y.L. and Zhang, S.S. (2018), "Compaction techniques and construction parameters of loess as filling material", *Geomech. Eng.*, **15**(6),1143-1151. https://doi.org/10.12989/gae.2018.15.6.1143.

Jiang, M.J., Zhang, F.G., Hu, H.J., Cui, Y.J. and Peng, J.B. (2014), "Structural characterization of natural loess and compacted loess under triaxial tests", *Eng. Geol.*, **181**, 249-260. https://doi.org/10.1016/j.enggeo.2014.07.021.

Jiang, T., Wang, L.J., Zhang, J.R., Jia, H. and Pan, J.S. (2020), "Effect of water content on near-pile silt deformation during pile driving using PIV technology", *Geomech. Eng.*, **23**(2), 139-149. https://doi.org/10.12989/gae.2020.23.2.139.

Jiang, Y., Chen, W.W., Wang, G.H., Sun, G.P. and Zhang, F.Y. (2016), "Influence of initial dry density and water content on the soil-water characteristic curve and suction stress of a reconstituted loess soil", *B. Eng. Geol. Environ.*, **76**(3), 1085-1095. https://doi.org/10.1007/s10064-016-0899-x.

Khalili, N. and Khabbaz, M.H. (1998), "A unique relationship for χ for the determination of the shear strength of unsaturated soils", *Geotechnique*, **48**(5), 681-687. https://doi.org/10.1680/geot.1998.48.5.681.

Leong, E.C. and Abuel-Naga, H. (2018), "Contribution of osmotic suction to shear strength of unsaturated high plasticity silty soil", *Geomech. Energy Environ.*, **15**, 65-73. https://doi.org/10.1016/j.gete.2017.11.002.

Li, R.J., Liu, J.D., Yan, R, Zheng, W. and Shao, S.J. (2014), "Characteristics of structural loess strength and preliminary framework for joint strength formula", *Water Sci. Eng.*, **7**(3), 319-330. https://doi.org/10.3882/j.issn.1674-2370.2014.03.007.

Liang, C.Y., Cao, C.S. and Wu, S.R. (2018), "Hydraulic-

mechanical properties of loess and its behavior when subjected to infiltration-induced wetting", *B. Eng. Geol. Environ.*, **77**(1), 385-397. https://doi.org/10.1007/s10064-016-0943-x.

Liang, Q.G., Li, J., Wu, X.Y. and Zhou, A.N. (2016), "Anisotropy of Q_2 Loess in the Baijiapo Tunnel on the Lanyu Railway, China", *B. Eng. Geol. Environ.*, **75**(1), 109-124. https://doi.org/10.1007/s10064-015-0723-z.

Lu, N. (2016), "Generalized soil water retention equation for adsorption and capillarity", *J. Geotech. Geoenviron. Eng.*, **142**(10), 04016051. https://doi.org/10.1061/(ASCE)GT.1943-5606.0001524.

Lu, X., Zhou, A.N., Shen, S.L., Li, J. and Sheng, D.C. (2020), "A micro-mechanical model for unsaturated soils based on DEM", *Comput. Meth. Appl. Mech. Eng.*, **368**, 113183. https://doi.org/10.1016/j.cma.2020.113183.

Ma, F.L., Yang, J. and Bai, X.H. (2017), "Water Sensitivity and Microstructure of Compacted Loess", *Transport. Geotech.*, **11**, 41-56. https://doi.org/10.1016/j.trgeo.2017.03.003.

Maleksaeedi, E. and Nuth, M. (2019), "Evaluation of capillary water retention effects on the development of the suction stress characteristic curve", *Can. Geotech. J.*, **57**(10), 1439-1452. https://doi.org/10.1139/cgj-2019-0326.

Mei, Y., Hu, C.M., Yuan, Y.L., Wang, X.Y. and Zhao, N. (2016), "Experimental study on deformation and strength property of compacted loess", *Geomech. Eng.*, **11**(1), 161-175. https://doi.org/10.12989/gae.2016.11.1.161.

Mu, Q.Y., Dong, H., Liao, H. J., Dang, Y.G. and Zhou, C. (2020), "Water-retention curves of loess under wetting drying cycles", *Geotech. Lett.*, **10**(1), 1-6. https://doi.org/10.1680/jgele.19.00025.

Ng, C.W.W., Sadeghi, H. and Jafarzadeh. F. (2017), "Compression and shear strength characteristics of compacted loess at high suctions", *Can. Geotech. J.*, **54**(5), 690-699. https://doi.org/10.1139/cgj-2016-0347.

Ng, C.W.W., Sadeghi, H., Jafarzadeh, F., Sadeghi, M., Zhou, C. and Baghbanrezvan, S. (2020), "Effect of microstructure on shear strength and dilatancy of unsaturated loess at high suctions", *Can. Geotech. J.*, **57**(2), 221-235. https://doi.org/10.1139/cgj-2018-0592.

Oberg, A. and Sallfors, G. (1997), "Determination of shear strength parameters of unsaturated silts and sands based on the water retention curve", *Geotech. Test. J.*, **20**, 40-48. https://doi.org/10.1520/GTJ11419J.

Pu, X., Wan, L. and Wang, P. (2021), "Initiation mechanism of mudflow-like loess landslide induced by the combined effect of earthquakes and rainfall", *Nat Hazards*, **105**(3), 3079-3097. https://doi.org/10.1007/s11069-020-04442-6.

Qiao, Y.F., Tuttolomondo, A., Lu, X.B., Laloui, L. and Ding, W.Q. (2020), "A generalised water retention model with soil fabric evolution", *Geomech. Energy Environ.*, **25**(2), 100205. https://doi.org/10.1520/GTJ20130034.

Rahardjo, H., Satyanaga, A., Mohamed, H.,Yee Ip, S.C. and Shah, R.S. (2019), "Comparison of soil-water characteristic curves from conventional testing and combination of small-scale centrifuge and dew point methods", *Geotech. Geol. Eng.*, **37**(2), 659-672. https://doi.org/10.1007/s10706-018-0636-2.

Satyanaga, A., Rahardjo, H., Koh, Z.H. and Mohamed, H. (2019), "Measurement of a soil-water characteristic curve and unsaturated permeability using the evaporation method and the chilled mirror method", *J. Zhejiang Univ. Sci. A Appl. Phys. Eng.*, **20**(5), 368-374. https://doi.org/10.1631/jzus.A1800593.

Sheng, D.C., Zhou, A.N. and Fredlund. D.G. (2011), "Shear strength criteria for unsaturated soils", *Geotech. Geol. Eng.*, **29**(2), 145-15. https://doi.org/10.1007/s10706-009-9276-x.

Sun, D.A., Gao, Y., Zhou, A.N. and Sheng, D.C. (2016), "Soil-water retention curves and microstructures of undisturbed and compacted Guilin lateritic clay", *B. Eng. Geol. Environ.*, **75**(2), 781-791. https://doi.org/10.1007/s10064-015-0765-2.

Sun, D.A., Matsuoka, H., Yao, Y. and Ichihara W. (2000), "An elasto-plastic model for unsaturated soil in three-dimensional stresses", *Soils Found.*, **40**(3), 17-28. http://doi.org/10.3208/sandf.40.3_17.

Sun, D.A., Sun, W.J. and Xiang, L. (2010), "Effect of degree of saturation on mechanical behaviour of unsaturated soils and its elastoplastic simulation", *Comput. Geotech.*, **37**(5), 678-688. https://doi.org/10.1016/j.compgeo.2010.04.006.

Sun, D.A., Zhang, J.R., Gao, Y. and Sheng, D.C. (2016), "Influence of suction history on hydraulic and stress-strain behavior of unsaturated soils", *Int. J. Geomech.*, **16**(6), 1-9. https://doi.org/10.1061/(ASCE)GM.1943-5622.0000602.

Sun, H.Q., Mašín, D., Najser, J., Neděla, V. and Navratilova, E. (2019), "Bentonite micro-structure and saturation evolution in wetting-drying cycles evaluated using ESEM, MIP and WRC measurements", *Geotechnique*, **69**(8), 713-726. https://doi.org/10.1680/jgeot.17.p.253.

Sun, W.J., Sun, D.A. and Liu, S.Q. (2014), "Hydro-mechanical behaviour of GMZ Ca-bentonite at high suctions", *Chin. J. Geotech. Eng.*, **36**(2), 346-353. https://doi.org/10.11779/CJGE201402012.

Tekinsoy, M.A., Kayadelan, C., Keskin, M.S. and Söylemez, M. (2004), "An equation for predicting shear strength envelope with respect to matric suction", *Comput. Geotech.*, **31**(7), 589-593. https://doi.org/10.1016/j.compgeo.2004.08.001.

Vanapalli, S.K., Fredlund, D.G., Pufahl, D.E. and Clifton A.W. (1996), "Model for the prediction of shear strength with respect to soil suction", *Can. Geotech. J.*, **33**(3), 379-392. https://doi.org/10.1139/t96-060.

Wang, H.K., Qian, H., Gao, Y.Y. and Li, Y.B. (2020), "Classification and physical characteristics of bound water in loess and its main clay minerals", *Eng. Geol.*, **265**, 105394. https://doi.org/10.1016/j.enggeo.2019.105394.

Wu, S.S., Zhou, A.N., Li, J., Kodikara, J., and Cheng, W.C. (2019) "Hydromechanical behaviour of overconsolidated unsaturated soil in undrained conditions", *Can. Geotech. J.*, **56**(11), 1609-1621. https://doi.org/10.1139/cgj-2018-0323.

Xu, X. Zhao, C.G. and Cai, G.Q. (2018), "Shear strength of unsaturated soils considering capillary and adsorptive mechanisms", *Rock Soil Mech.*, **39**(6), 2059-2064, 2072. https://doi.org/10.16285/j.rsm.2017.1727.

Zhang, C. and Lu, N. (2021), "Closure to "unified effective stress equation for soil" by Chao Zhang and Ning Lu", *J. Eng. Mech.*, **147**(2), 07020004. https://doi.org/10.1061/(ASCE)EM.1943-7889.0001893.

Zhang, J.R., Niu, G., Li, X.C. and Sun, D.A. (2020), "Hydro-mechanical behavior of expansive soils with different dry densities over a wide suction range", *Acta Geotech.*, **15**(1), 265-278. https://doi.org/10.1007/s11440-019-00874-y.

Zhang, J.R., Sun D.A. and Jiang, T. (2016), "Shear strength of weakly expansive soils and its prediction in a wide range of suction", *Chin. J. Geotech. Eng.*, **38**(6), 1064-1070. https://doi.org/10.11779/CJGE201606013.

Zhang, J.W., Mu, Q.Y., Garg, A., Liu, F.L. and Cao, J. (2020), "Shear behavior of unsaturated intact and compacted loess: A comparison study", *Environ. Geol.*, **79**(3), 79. https://doi.org/10.1007/s12665-020-8820-0.

Zhang, Y., Zhao, Y, Liu, J., Meng, T.Y., Shao, S.J. and She, S.T. (2021), "An experimental study on the deformation and strength characteristics of Q3 loess under a plain strain anisotropic consolidation condition", *Adv. Civ. Eng.*, 1-13. https://doi.org/10.1155/2021/8813707.

Zhao, C.G., Liu, Z.Z., Shi, P.X., Li, J., Cai, G.Q. and Wei, C.F. (2016), "Average soil skeleton stress for unsaturated soils and discussion on effective stress", *Int. J. Geomech.*, **16**(6), D4015006.

https://doi.org/10.1061/(ASCE)GM.1943-5622.0000610.
Zhou, A.N., Huang, R.Q. and Sheng, D.C. (2016), "Capillary water retention curve and shear strength of unsaturated soils", *Can*. *Geotech*. *J*., **53**(6), 974-987. https://doi.org/10.1139/cgj-2015-0322.
Zhou, A.N. and Sheng, D.C. (2015), "An advanced hydro-mechanical constitutive model for unsaturated soils with different initial densities", *Comput*. *Geotech*., **63**, 46-66. https://doi.org/10.1016/j.compgeo.2014.07.017.
Zhou, A.N., Sheng, D.C., Sloan, S.W. and Gens, A. (2012), "Interpretation of unsaturated soil behavior in the stress-saturation space. I: Volume change and water retention behaviors", *Comput*. *Geotech*., **43**(3), 178-187. https://doi.org/10.1016/j.compgeo.2012.04.010.
Zhou, A.N., Wu, S.S., Li, J., and Sheng, D.C. (2018), "Including degree of capillary saturation into constitutive modelling of unsaturated soils", *Comput*. *Geotech*., **95**(10), 82-98. https://doi.org/10.1016/j.compgeo.2017.09.017.

CC